http://www.sjst.psu.ac.th

Original Article

Effects of cooling rate on impact properties and microstructure of gray cast iron ASTM A48

Ganwarich Pluphrach[1*], Sombat Teekasap[2], Tirawat Amornthatri[3],
Teerapath Limboonruang[1], Tri Kharanan[1], and Kanviroon Pluphrach[4]

[1] *Department of Mechanical Engineering, Faculty of Engineering,*
Srinakharinwirot University, Ongkharak, Nakhon Nayok, 26120 Thailand

[2] *Faculty of Science and Technology,*
Thonburi University, Nong Khaem, Bangkok, 10160 Thailand

[3] *Bangkok Sheet Metal Public Co., Ltd.,*
Phra Padaeng, Samut Prakarn, 10130 Thailand

[4] *Research Center for Mechanical Engineering and Business Economics,*
Ganwarich R&D Co., Ltd., Nong Khaem, Bangkok, 10160 Thailand

Abstract

In this study, gray cast iron ASTM A48 was subjected (1) to testing for effects of cooling rate on its impacts properties; and (2) to assessing the relationship between microstructure and properties. The cooling rate was varied by testing the four cooling methods (1) As-cast; (2) Furnace-cooled; (3) Air-cooled; and 4) Green sand-cooled. It was found that the impacted properties are governed by flat fractures that meet minimum energy density criteria. Thus, we established a correlation between the microstructure and impact properties of GI ASTM A48 for conformance analysis to develop a predictive relationship. These include test specimen size and energy consumption patterns. As a result, the impact properties of GI ASTM A48 are finally predictable. This results in good efficiency and can be applied to heat treatments of some new materials.

Keywords: impact behavior, systematic relationship, integrity of cooling rate, gray cast iron ASTM A48

1. Introduction

Compared with steels and other cast irons, GI ASTM A48 has superior mechanical properties such as high machinability, vibration adsorption, and castability. In manufacture of gears, guide rails, camshafts, and engine liners for diesel engines GI ASTM A48 is widely used because it is inexpensive and easy to use (Keller *et al*., 2007; Lombardi, Ravindran, Sediako & MacKay, 2014; Morton & Watson, 1974; Saeidi *et al*., 2017; Truhan, Qu, & Blau, 2005). Contact

behavior is an outstanding feature of GI ASTM A48 when external forces are transmitted by surfaces of the mechanical components. In addition, GI ASTM A48 exhibits an excellent combination of strength and fracture resistance, making it widely used in engineering applications (Aslantaş, Talaş, & Taşgetiren, 2004; Berto, Cendón, & Elices, 2016; Fu *et al*., 2018). High strength and good ductility are among key characteristics of structural engineering materials that are known to be contradictory.

The matrix structure and morphology of graphite play essential roles in the properties of GI ASTM A48 in the context of this study. In high-quality GI ASTM A48 polishing, its surface is characterized by multiple graphite flakes, as shown in Figure 1. The graphite particles are flakes

---

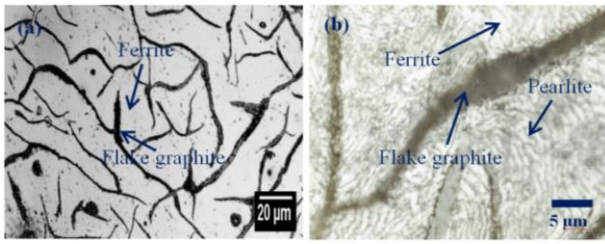*Corresponding author
Email address: pganwarich@yahoo.com

Figure 1. Photomicrograph of flake graphite: (a) in the as-cast GI ASTM A48 (Ferritic) used in general industry; (b) microstructure of as-received GI ASTM A48 (Ferrito-pearlitic) with scale bars indicating the magnification levels.

of gray cast iron, measuring up to 50% vol. (Mazloum, Oddone, Reich & Sevostianov, 2019). Factors influencing flake graphite formation (Park & Verhoeven, 2019) include adding a substance that accelerates the separation of carbon from cementite (Si), section size, and cooling rate. The interplay of these factors influences the resulting matrix structure. The cooling rate-oriented heat treatment can influence mechanical behavior in various aspects, such as hardness, tensile strength, and impact resistance. In addition, these aspects are related to the primary dendrite arm spacing, secondary dendrite arm spacing, and the ferrite's thickness and cementite layer influenced by the cooling rate (Behnam, Davami & Varahram, 2019). The objective of this study was to characterize the effects of holding time and cooling rate in four treatment categories on impact behavior: 1) As-cast, 2) Furnace-cooled (FC), 3) Air-cooled (AC), and 4) Greensand-cooled (GC), as shown in Figure 2 (Megahed, El-Kashif, Shash & Essam, 2019; Wang *et al.*, 2020). The GI ASTM A48 material has some prior cooling rate related results from microstructural studies and technical tests involving sand casting using a variety of modules (Behnam, Davami & Varahram, 2010).
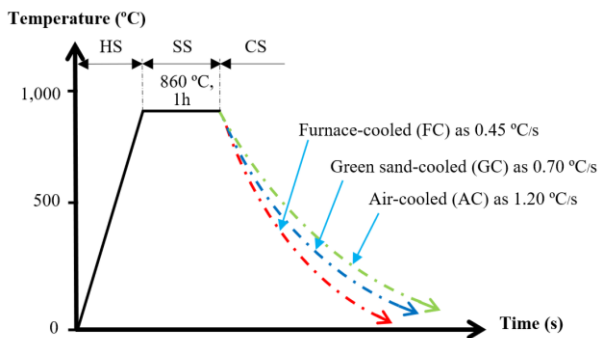

Figure 2. Testing of heating and cooling rate effects on the GI ASTM A48 specimens from Y-block sand casting show starting the heating from room temperature to the austenitizing 860°C as heating section (HS), holding this temperature as a soaking area (SS), and then using alternative cooling rates in the cooling section (CS) through the transformation range: FC as annealing in a closed electric resistance furnace cooled by switching off the supply; GC as in green sand cooled; and AC as in air-cooled

2. Materials and Methods

In the experiments, GI ASTM A48 material is cast in a green sand mold known as Y-block sand casting; this can be considered as an example in the Y block foundry industry specified in ASTM A48/A48M-03(2016) or A536-84(2019) e1, as shown in Figure 3(a). GI ASTM A48 samples were made by the National Center for Metal and Materials Technology, Thailand. Four different samples were produced, requiring a medium frequency induction furnace with a maximum output power of 15 kW, a frequency range of 1-20 kHz, in the preparation of GI ASTM A48, which requires steel scrap and suitable iron ingots for the detailed chemical composition shown in Tables 1 and 2. In addition, the pouring time must be taken into account as all samples take approximately 15.50 minutes on average (Álvarez, Luis & Puertas, 2004; ELSawy, EL-Hebeary, El Mahallawi, 2017; Janerka *et al.*, 2014; Sadeghi, Moloodi, Golestanipour & Shahri, 2017; Uzun, 2019). This enables a more accurate analysis of the ingredients, affecting the data shown in Table 3. This solidification produces interconnected graphite flakes, which resemble several potato crisps glued together at a single location. The point at which the flakes are connected is the original graphite nucleus. GI ASTM A48 contains many clusters or eutectic cells of graphite flakes, with each cell representing one nucleation event of liquid to graphite+austenite. Inoculation, produced by adding small amounts of ferrosilicon alloy or by rapid late cooling, helps make more acceptable eutectic cells, thus improving the casting strength. However, the graphite flakes have low mechanical strength and are brittle, so they are considered equivalent to tiny cracks within the pearlite matrix. Hence this material has an elongation of only about 1%.

Microstructure analysis uses various types of microscopy to observe the morphology of graphite and matrix. The phases present after transformation are determined by optical microscopy (OM); images (1360 x 2048 px) of droplet formation were recorded with a Nikon D90 attached to a Zeiss Axiolab optical microscope. The shutter speed was set at 1/4000, and the f-number was fixed at 5.6. To prevent contamination, the entire set-up was placed in a laminar flow cabinet (CaptAir Filterair 936). Electron backscatter diffraction (EBSD) analysis in scanning electron microscopy (SEM) is used to characterize the structure by revealing grain boundaries, phase boundaries, inclusion distributions, fragmentation, and evidence of mechanical deformation (Guitar *et al.*, 2020). Metallurgical examination of matrix and graphite structures can be performed following the EBSD or ISO 945 standard method (Kante & Leineweber, 2018; Vértesy *et al.*, 2015) and ASTM E562-05e1 test method (Konoplyuk, 2010). SEM with SEM SUPRA 55 VP (Carl Zeiss AG, Oberkochen, Germany) was used for maximal clarity to enable linking the observations of material properties with the fracture morphology. There are five types of flake graphite (by their patterns), defined by the letters A through E. The sample in Figure 1 can be considered as type A (Abreu, Sundberg, Elfsberg & Jonsson, 2020; Li, *et al.*, 2019; Liu *et al.*, 2020). The percent pearlite in the matrix was obtained by comparing the photographic versus the reference ferrite-pearlite percentage graph proposed by the American Foundrymen's Society Quality Control Committee.
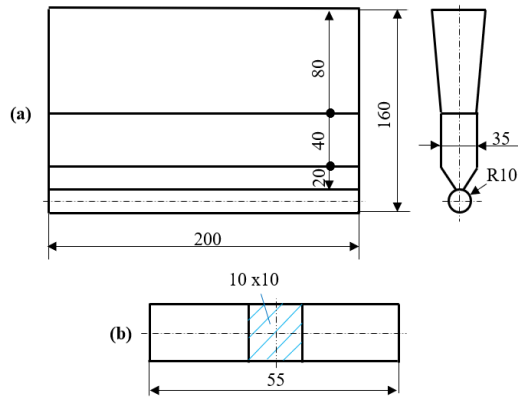
Figure 3. Dimensions of (a) the Y-block sand casting employed in this research study; (b) mechanical specimen for metallographic analysis and testing of impact strength (unit is mm, not to scale)

Table 1. Compositions of the scrap steel and iron ingots used in this study (wt%).

	C	Si	Mn	P	S	Cu
Steel scrap	0.20	0.80	1.28	0.015	0.027	0.19
Iron ingot	3.90	1.50	0.30	0.022	0.015	-

Mechanical test specimens for metallurgical analysis and testing were subjected to impact testing using a Roell Amsler RKP-450 Charpy impact tester (Zwick/Roell). The pendulum's speed was 5.24m/s, and the test was performed at room temperature. This was done in order to analyze the influences of heat treatment on the impact behavior of ASTM A48 gray cast iron. Charpy low-temperature specimen testing determines the material's toughness, impact resistance, and brittleness. Therefore, multiple tests are needed to assess the impact strength of some materials. Figure 3(b) shows an unnotched specimen according to ASTM-A327M. A most critical consideration with small-sized samples is to clarify the effects of size on the test results. Size effects on determining the ductile-to-brittle transition temperature (DBTT) in the Charpy impact test have been reported (Kurita *et al.*, 2004). In the Charpy impact testing, the process of cleavage fracture is considered to consist of three steps. (1) Plastic deformation, which involves the pile-up of dislocations along their slip

planes at an obstacle: definite evidence of crack nucleation by plastic flow has been found in the bcc transition metals, as shown in Figure 4., (2) Crack initiation, and (3) crack propagation. To perform a hardness test, we used a Wilson Hardness brand Rockwell B-Scale (HRB) hardness tester that withstands up to 100 kg major load. Testing used a 1/16" diameter steel ball HRB with dwell time of 6.0 seconds.
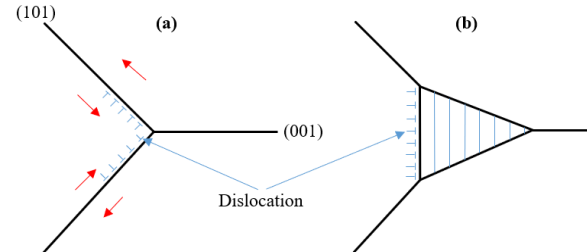

Figure 4. In the bcc structure: (a) motion of dislocation on intersecting {110} planes; (b) resulting in the nucleation of a void, which forms a crack on a {100} plane

3. Results and Discussion

3.1 Microstructure

Microstructures of As-cast, FC, AC, and GC materials with EBSD images for the different cooling rates are shown in Figures 5 and 6. The graphite and Fe_3C phase fractions in the matrix of all relevant specimens and their mechanical properties are shown in Table 3. The resulting fraction of graphite phase was determined from the analysis in Figures 5 and 6. To influence the impact strength behavior prediction in Table 3 and consider ingredients such as the percentage of silicon, it is also possible to consider heat treatment effects via the cooling rates. Based on the graphite and Fe_3C phase fractions analysis, we can explain how impact forces are affected. According to Table 3, for the range of As-cast cooling rate on considering the impact strength, only the 2.98 J corresponds to graphite phase fraction at 7.76% and Fe_3C phase fraction at 24.96% according to the EBSD correlation, as shown in Figure 6. Finally, we can collect the cooling rate effect on phase fraction and mechanical properties of GI ASTM A48 material, as shown in Figure 7. With the least graphite phase fraction, since any heat source has not treated the specimen to affect the carbon atoms for the Fe_3C

Table 2. Chemical composition of as-cast GI ASTM A48 (wt%)

C	Si	Mn	P	S	Cu	Al	Ni	Cr	Mo	Ti
3.12	2.02	0.30	0.044	0.19	0.24	-	0.04	0.11	0.035	0.012

Table 3. Microstructures and mechanical properties of the GI ASTM A48 samples

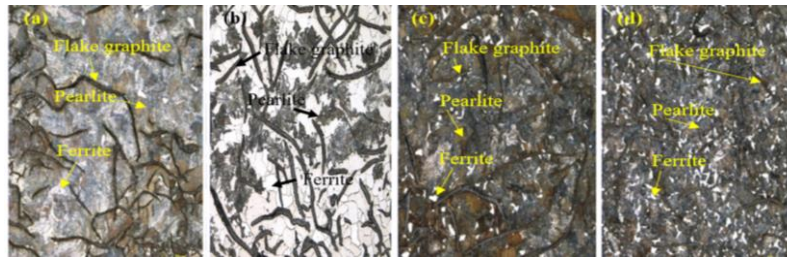| Cooling rate	Graphite phase fraction (%)	Fe_3C phase fraction (%)	Rockwell B-Scale (HRB)	Elongation (%)	Impact strength (J)
As-cast	7.76	24.96	95.8	1.08	2.98
FC	24.57	11.64	85.2	1.03	4.06
AC	16.77	6.62	94.7	1.00	4.82
GC	20.77	6.35	97.0	1.04	4.52

Figure 5.   The microstructures of the different cooling rate cases: (a) As-cast; (b) FC; (c) AC; and (d) GC. All the four figures have the same scale, with 20 microns shown by scale bar.
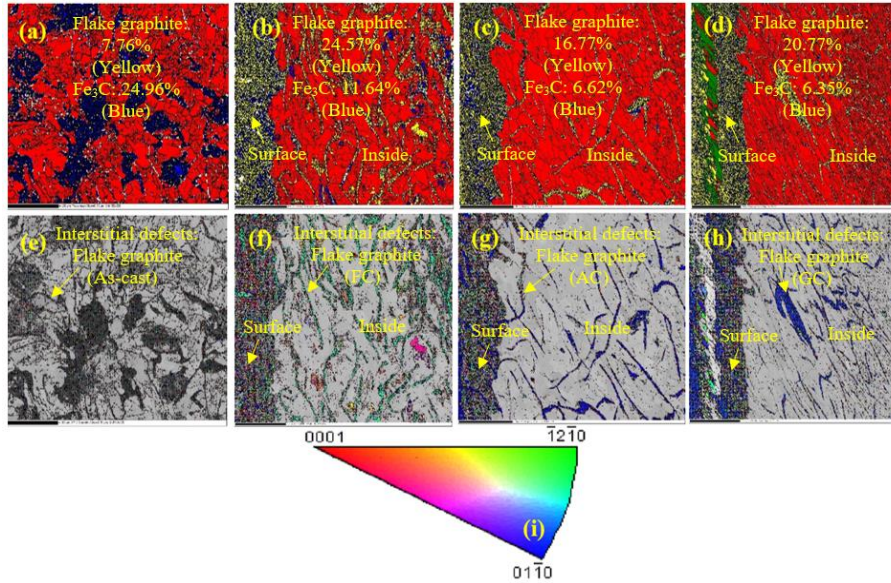

Figure 6.   The EBSD images of different cooling rate cases. Top row shows phase maps: (a) As-cast; (b) FC; (c) AC; (d) GC; and bottom row IPF Z graphite: (e) As-cast; (f) FC; (g) AC; (h) GC; In (i) an inverse pole figure maps for graphite as maximally about 24.57% phase fraction which is characteristic of FC.
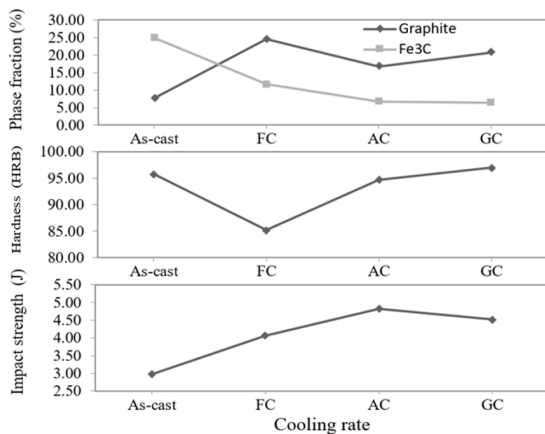

Figure 7.   Effects of cooling rate on the phase fractions and mechanical properties of the GI ASTM A48 cases

separation, the impact value strength is the lowest, as shown. When heat is applied to the sample, as shown in the FC, the carbon atoms are separated from the Fe_3C, with silicon support, which reduces the Fe_3C phase fraction to 11.64%. The graphite phase fraction increased to 24.57% as the carbon decomposed from Fe_3C to form graphite roses, and the cooling rate within the heat treatment furnace was slow, approximately 0.45 ºC/s, as shown in Figure 2, resulting in the lowest hardness of the FC case among the samples. Thus, the Fe_3C content maximizes the graphite content as shown; therefore, impact strength increased to 4.06 J. The AC case has a cooling rate of 1.20 ºC/s (Figure 2), and the reduced content of Fe_3C and graphite phase fraction are 6.62 and 16.77%, in Table 3, with the consequences seen in Figure 7. This is due to more significant carbon dissociation at FC cooling rate, and less graphite formation with AC than with FC, thus impact strength increased to 4.82 J. Lastly, the GC case has the same explanation as AC, but because the slower cooling is at 0.70 ºC/s making Fe_3C, graphite phase fraction, and impact strength 6.35%, 20.77%, and 4.52 J, respectively.

3.2 Mechanical properties

Table 3 shows the various mechanical properties of GI ASTM A48 in this examination. This corresponds to the schematic representation of the nature of the cooling rate's effect on the mechanical properties of GI ASTM A48 in Figure 7. As mentioned above, the Rockwell B-Scale hardness properties and elongation changed slightly for GI ASTM A48

with the various cooling rates. Likewise, if the cooling rate is adjusted, it will not cause a significant change in the mechanical properties elongation that is slightly increased, or the hardness that decreases. With other analyses, contrary to the above, the cooling rate effects on graphite morphology and Fe_3C structure caused significant changes, and in impact strength it was evident that AC had the highest 4.82 J, followed by GC, FC and As-cast at 4.52, 4.06, and 2.98 J, as shown in Table 3 and Figure 7. Considering the impact behavior, the cooling rate modifications changed the impact strength according to the cooling rate design. However, when analyzing the design levels of AC, GC, and FC concerning the fractional graphite phase, except for As-cast, those impact strength values were lowered to 4.82, 4.52, and 4.06 J, respectively. In an impact specimen fracture test, the more the graphite is interconnected, the easier it is to propagate cracks. The increased percentage of the graphite phase fraction is also considered consistent with the Fe_3C content, which leads to a lower impact strength. According to Table 3, the characteristics of the change in hardness and elongation cannot be identified as equal to the impact value. However, the increased graphite and Fe_3C phase fraction are still considered to reduce sufficient weight.

Therefore, the relationship between impact strength and hardness can be characterized using Figure 7 and Table 3, considering the cooling rate primarily affecting the impact force results when it changes from As-cast to FC. For example, it increased from 2.98 J to 4.06 J, and vice versa, hardness decreased from 95.8 HRB to 85.2 HRB due to FC having a new level of atomic bond strength. For this reason, when FC levels are adjusted to AC and GC cases, the impact strength and hardness increased and decreased, as indicated in both the figure and the table.

3.3 Fracture surface analysis

Figure 8 shows fracture surfaces on broken halves of the Charpy impact specimens that were prepared at different cooling rates. They were observed and analyzed

systematically, taking this material at AC as an example. The AC sample shows the highest impact strength; it is reasonable according to the fracture surface analysis. Also, SEM images of the specimen after the Charpy impact test results are displayed. Considering Figure 8(a), it can be further explained that the shear and flat fracture zones are derived from the macroscopic fracture surface. Additionally, in Figure 8(b) crack initiation zone and in Figure 8(c) crack propagation zone both come from the flat fracture zone. The impact energy analysis can be based on the initial crack zone in Figure 8(b), in which a large number of small river patterns are present, indicating that these took up the majority of the impact energy (Liu *et al.*, 2017). Cracks are most readily propagated along specific crystallographic planes, usually, the {100} plane, by the transgranular manner cleavage shown in Figure 8(c). Another figure shows ductile fracture mode in the shear fracture zone in Figure 8(d) with small/shallow dimples. The analysis of these image data taken at sufficient magnification observed the flow of fibers and river patterns with the cleavage facets. Thus, there was a mixed ductile-brittle fracture mode available in FC, AC, and GC cases of the GI ASTM A48.

4. Conclusions

In this study in the flake graphite patterns, the effects of cooling rate associated with the impact behavior of GI ASTM A48 are summarized as follows:

1. The energy failure criterion is generally determined by the evolution of plastic deformation, crack nucleation, and growth; characterizing the successive stages in fracture. This paper shows that toughness represents competition between flat and shear fractures, following the minimum energy density criterion.

2. Unnotched impact resistance of this study measured both the energy to form the crack and the strength to grow the damage and break the specimen. It is often the most relevant because in real life mechanical parts are usually not notched.
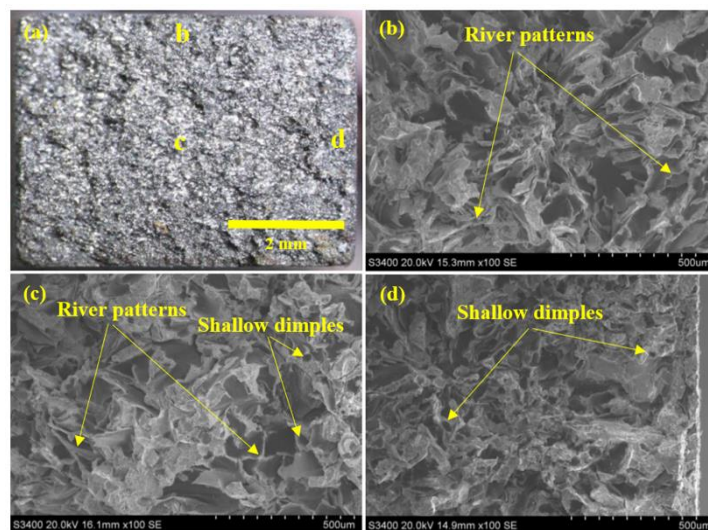

Figure 8.   The transgranular cleavage fracture surface of the AC Charpy impact specimen: (a) macroscopic fracture surface; (b) crack initiation zone; (c) crack propagation zone; and (d) shear fracture zone

3. Modification of the cooling rate resulted in modifications to graphite and Fe3C, affecting impact resistance. In this study, as-cast impact resistance was minimal with lack of heat treatment, so it was seen that AC had the highest impact resistance due to the lower graphite phase fraction than in GC and FC. Although AC has the highest impact resistance, its hardness is less than that of GC because it has a higher elongation than GC.

Acknowledgements

References

Aslantaş, K., Talaş, S., & Taşgetiren, S. (2004). Fracture of a compressor rotor made from grey cast iron. *Engineering Failure Analysis, 11*(3), 369-373.

Álvarez, L., Luis, C. J., & Puertas, I. (2004). Analysis of the influence of chemical composition on the mechanical and metallurgical properties of engine cylinder blocks in grey cast iron. *Journal of Materials Processing Technology, 153*(1), 1039-1044.

Abreu, M., Sundberg, J., Elfsberg, J., & Jonsson, S. (2020). Morphology and mechanisms of cavitation damage on lamellar gray iron surfaces. *Wear, 456-457*, 203324.

Berto, F., Cendón, D. A., & Elices, M. (2016). Fracture behavior under torsion of notched round bars made of gray cast iron. *Theoretical and Applied Fracture Mechanics, 84*, 157-165.

Behnam, M. M. J., Davami, P., & Varahram, N. (2010). Effect of cooling rate on microstructure and mechanical properties of gray cast iron. *Materials Science and Engineering: A, 528*(2), 583-588.

ELSawy, E. E. T., EL-Hebeary, M. R., & El Mahallawi, I. S. E. (2017). Effect of manganese, silicon and chromium additions on microstructure and wear characteristics of grey cast iron for sugar industries applications. *Wear, 390-391*, 113-124.

Fu, B., Fu, L., Liu, S., Wang, H. R., Wang, W. & Shan, A. (2018). High strength-ductility nano-structured high manganese steel produced by cryogenic asymmetry-rolling. *Journal of Materials Science and Technology, 34*(4), 695-699.

G. Uzun, G. (2019). Analysis of grey relational method of the effects on machinability performance on austempered vermicular graphite cast irons. *Measurement, 142*, 122–130.

Guitar, M. A., Scheid, A., Nayak, U. P., Nakamura, L., Ponge, D., Britz, D., & Mücklich, F. (2020). Quantification of the phase transformation kinetics in high chromium cast irons using dilatometry and metallographic techniques. *Metallurgical and Materials Transactions A: Physical Metallurgy and Materials Science, 51*, 3789-3801.

Janerka, K., Pawlyta, M., Jezierski, J., Szajnar, J., & Bartocha, D. (2014). Carburiser properties transfer into the structure of melted cast iron. *Journal of Materials Processing Technology, 214*(4), 794-801.

Keller, J., Fridrici, V., Kapsa, Ph., Vidaller, S., & Huard, J. F. (2007). Influence of chemical composition and microstructure of gray cast iron on wear of heavy-duty diesel engines cylinder liners. *Wear, 263*(7-12), 1158–1164.

Kurita, H., Yamamoto, T., Marui, M., Suwarno, H., Yoshitake, T., Yano, Y., . . . Matsui, H. (2004). Specimen size effects on ductile-brittle transition temperature in Charpy impact testing. *Journal of Nuclear Materials, 329-333*(B), 1107-1112.

Kante, S., & Leineweber, A. EBSD characterization of the eutectic microstructure in hypoeutectic Fe-C and Fe-C-Si alloys. *Materials Characterization, 138*, 274-83,

Konoplyuk, S. (2010). Estimation of pearlite fraction in ductile cast irons by eddy current method. *NDT and E International, 43*(4), 360–64.

Lombardi, A., Ravindran, C., Sediako, D., & MacKay, R. (2014). Determining the mechanism of in-service cylinder distortion in aluminum engine blocks with cast-in gray iron liners. *Metallurgical and Materials Transactions A: Physical Metallurgy and Materials Science, 45*, 6291-6303.

Liu, Y., Martinón-Torres, M., Mei, J., Sun, W., Shao, A., & Chen, K. (2020). Cast a different iron: Grey and mottled cast iron production in early China. *Journal of Cultural Heritage, 46*, 184-192.

Li, Y., Dong, S., Yan, S., Liu, X., Li, E., He, P., & Xu, B. (2019). Elimination of voids by laser remelting during laser cladding Ni based alloy on gray cast iron. *Optics and Laser Technology, 112*, 30-38.

Morton, K., & Watson, P. (1974). The low-cycle fatigue behaviour of grey cast iron and its application to fatigue problems in diesel engine cylinder liners. *Metals Technology, 1*(1), 258-264.

Mazloum, A., Oddone, V., Reich, S., & Sevostianov, I. (2019). Connection between strength and thermal conductivity of metal matrix composites with uniform distribution of graphite flakes. *International Journal of Engineering Science, 139*, 70-82.

Megahed, H., El-Kashif, E., Shash, A. Y., & Essam, M. A. (2019). Effect of holding time, thickness and heat treatment on microstructure and mechanical properties of compacted graphite cast iron. *Journal of Materials Research and Technology, 8*(1), 1188-1196.

Park, J. S., & Verhoeven, J. D. (1996). Transitions between type A flake, type D flake, and coral graphite eutectic structures in cast irons. *Metallurgical and Materials Transactions A: Physical Metallurgy and Materials Science, 27*, 2740-2753.

Saeidi, F., Taylor, A. A., Meylan, B., Hoffmann, P., & Wasmer, K. (2017). Origin of scuffing in grey cast iron-steel tribo-system. *Materials and Design, 116*(15), 622-630.

Sadeghi, A., Moloodi, A., Golestanipour, M., & Shahri, M. M. (2017). An investigation of abrasive wear and corrosion behavior of surface repair of gray cast iron by SMAW. *Journal of Materials Research and Technology, 6*(1), 90–95.

Truhan, J. J., Qu, J., & Blau, P. J. (2005). A rig test to measure friction and wear of heavy duty diesel engine piston rings and cylinder liners using realistic lubricants. *Tribology International, 38*(3), 211-218.

Vértesy, G., Uchimoto, T., Takagi, T., Tomáš, I., & Kage, H. (2015). Nondestructive characterization of flake graphite cast iron by magnetic adaptive testing. *NDT and E International, 74*, 8-14.

Wang, B., Pan, Y., Liu, Y., Lyu, N., Barber, G. C., Wang, R., . . . Hu, M. (2020). Effects of quench-tempering and laser hardening treatment on wear resistance of gray cast iron. *Journal of Materials Research and Technology, 9*(4), 8163-8171.